Multispectral Optical Confusion System: Visible to Infrared Coloration with Fractal Nanostructures

Injoong Chang[a], Taehwan Kim[b], Namkyu Lee[c], Juyeong Nam[a], Joon-Soo Lim[a], Maroosol Yun[a], and Hyung Hee Cho[a*]

a. Department of Mechanical Engineering, Yonsei University, 50 Yonsei-ro, Seodaemun-gu, Seoul, 03722, Koreac.

b. Semiconduction R&D Center, Samsung Electronics Co., Ltd., 1, Samsungjeonja-ro, Hwaseong-si, Gyeonggi-do, 18488, Korea

c. IBI-4, Forschungszentrum Juelich GmbH, Wilhelm-Johnen-Straße, 52425 Jülich, Germany.

* Corresponding author

Tel.: +82 2 2123 2828

Fax: +82 2 312 2159

E-mail: hhcho@yonsei.ac.kr

Abstract

Optical confusion refers to a camouflage technique assimilated with the surroundings through manipulating colors and patterns. With the advances in multispectral imagery detection systems, multispectral camouflage studies on simultaneous deceptions in the visible to infrared ranges remain a key challenge. Thus, creating pixelated patterns is essential for mimicking background signatures by assimilating both colors and patterns. In this study, a multispectral optical confusion system (MOCS) comprising pixelated silicon-based fractal nanostructures (Si-FNSs) is introduced to realize multispectral optical confusion. We analyzed the fractality of the Si-FNSs to understand the relationships between structural characteristics and optical properties with the aggregation phenomenon. The aggregation phenomenon changes the morphological heterogeneity by up to 38.5%, enabling a controllable range of visible reflectivity from 0.01 to 0.12 and infrared emissivity from 0.33 to 0.90. Visible and infrared colors were obtained by controlling the wet-etching time from 10 to 240 min and temperature from 40 to 100 ℃. Finally, the MOCS consisting of pixelated Si-FNSs was designed and created by extracting the pattern from the simultaneously captured visible and infrared background images. Using the artificial backgrounds representing these images, we evaluated and compared the multispectral optical confusion performance of the MOCS with conventional camouflage surfaces.

Keywords

Optical confusion; Multispectral coloration; Fractal nanostructures; background; Pixelation;

1. Introduction

Camouflage refers to the ability to conceal oneself from predators through assimilation with the surrounding environment. Many creatures vary their appearances (e.g., colors and patterns) so as to blend in with their surroundings to achieve optical confusion effect.[1,2] With the advances in optical detection systems,[3–6] state-of-the-art detectors have been developed using high-resolution electro-optical or infrared image sensors that can be used for multispectral detection by fusing the signatures from the visible to infrared spectral ranges. Since these detectors have increased detection performance[7] and can even identify objects that cannot be seen with visible light (e.g., objects behind opaque walls),[6] research into multispectral camouflaging that simultaneously deceives in the visible to infrared ranges remains a key challenge.

To countermeasure novel detection systems, many researchers have studied various camouflage materials whose electromagnetic (EM) behaviors can be manipulated in particular spectral ranges. Since visible colors are generated by the reflection of visible light and infrared signatures are obtained from surface emissions based on temperature and emissivity[8], color filters with subwavelength structures have been studied extensively for controlling visible colors[2,9–12] as well as photonic or plasmonic resonators for controlling infrared signatures.[13–17]

Additionally, to address the EM properties in a multispectral range, several artificial materials have been studied, such as thin-film stacks,[1,18] hierarchical materials combining two or more materials working in different spectral ranges,[19–21] and metal-dielectric-metal (MDM) structures having broad tunable ranges.[22,23] Based on these materials, few recent studies have reported on multispectral camouflaging (e.g., visible to microwave,[18] visible to infrared,[9,22,24,25] infrared to microwave[21]) with the aim of lowering signature levels by assuming a constant-intensity background.[13–16,22]

However, considering the characteristics of the aforementioned state-of-the-art imagery detectors, signature lowering is not always effective owing to size contrast between the signature pattern of the target and surrounding background, independent of the low signature level.[26] Thus, optical confusion strategy is

essential over entire spectral ranges like the conventional visible camouflage pattern, which assimilates both colors and patterns with the surroundings by creating pixelated patterns.[27,28]

Although many studies have successfully manipulated the multispectral characteristics of materials,[1,19,20,24] creating camouflage patterns comprising pixels of multispectral camouflage materials is costly and time-consuming for practical use in large-scale device applications. One of the easiest methods of achieving manufacturability and mass production in material fabrication is by the wet-etching method.[29] Generally, the wet-etching method controls only one parameter, i.e., etching time, so most studies on materials based on the wet-etching method investigated the optical characteristics in only a single spectral range.[30–32] However, if the etching time is sufficiently lengthy, then surface morphological changes as well as shape variations in the depth direction can occur because of the forces between the generated nanostructures.[33,34] Additionally, although wet-etching methods inevitably generate fractal structures that exhibit high randomness and morphological heterogeneities, recent studies have reported that fractality could affect the optical properties, especially absorption, to enhance the light-trapping effect.[31,32] Therefore, we believed that silicon-based fractal nanostructures (Si-FNSs) could be potentially used to manipulate the multispectral optical properties by only controlling the etching time.

Herein, we proposed a novel optical confusion camouflage system with Si-FNS pixels for colorations in the visible and infrared ranges. We controlled the wet-etching time from 10 to 240 min for fabricating Si-FNSs to manipulate the reflectivity (0.01-0.12) in the visible range and emissivity (0.33-0.90) in the long-wavelength infrared (LWIR) range simultaneously. To understand the relationships between structural variations and optical characteristics in the etching process, we calculated and measured the fractality and optical properties in a multispectral range. Considering the application of optical confusing camouflage, the infrared signature is analyzed while increasing the hotplate temperature from 40 to 100°C, which represents the surface temperature determined by various environmental conditions. Moreover, we normalized the radiance of Si-FNSs to design the optical confusing camouflage surface regardless of surface temperature. Finally, we evaluated the multispectral optical confusion camouflage performance to

design and create a multispectral optical confusion system (MOCS) using artificial backgrounds assimilated with actual environmental images captured in the visible and infrared ranges.

2. Results and Discussion

2.1. Characteristics of silicon-based fractal nanostructures

Figure 1a schematically represents optical confusion camouflage by applying the MOCS to a human hand in both the visible and infrared ranges. As the etching time increases, the visible colors of the Si-FNSs vary from black to yellow, similar to the background colors. Simultaneously, the infrared signatures vary from low to high signature levels. Therefore, well-designed MOCSs consisting of pixelated Si-FNSs can display colors and patterns similar to the backgrounds regardless of the waveband. While the human hand is distinguishable from the background owing to the single visible color and high infrared signature (or high temperature), the MOCS-applied hand exhibits high multispectral camouflage performance in both visible and infrared backgrounds. Moreover, the MOCS exhibits potential for high pattern variability. By redesigning the camouflage patterns for new backgrounds and rearranging the Si-FNSs, a MOCS can achieve high optical confusion camouflage performance under various backgrounds.

Prior to creating the MOCS and evaluating its multispectral camouflage performance, we fabricated six types of Si-FNSs using the metal-assisted chemical etching (MaCE) method with etching times of 10, 30, 50, 70, 110, and 240 min. A plasma ashed 500-μm-thick silicon substrate was immersed in a seeding solution for 1 min to determine the etching locations randomly. Then, the seeded substrate was immediately immersed in the etchant solution to manipulate the heights of the Si-FNSs by controlling the immersion time (see Experimental section for details).

Figure 1b shows the top-view scanning electron microscope (SEM) images and angled-view structural schematic of the fabricated Si-FNSs. When observing the Si-FNSs under high magnification (×20,000), they seem like porous structures containing column-like silicon nanostructures and air cavities. Naturally,

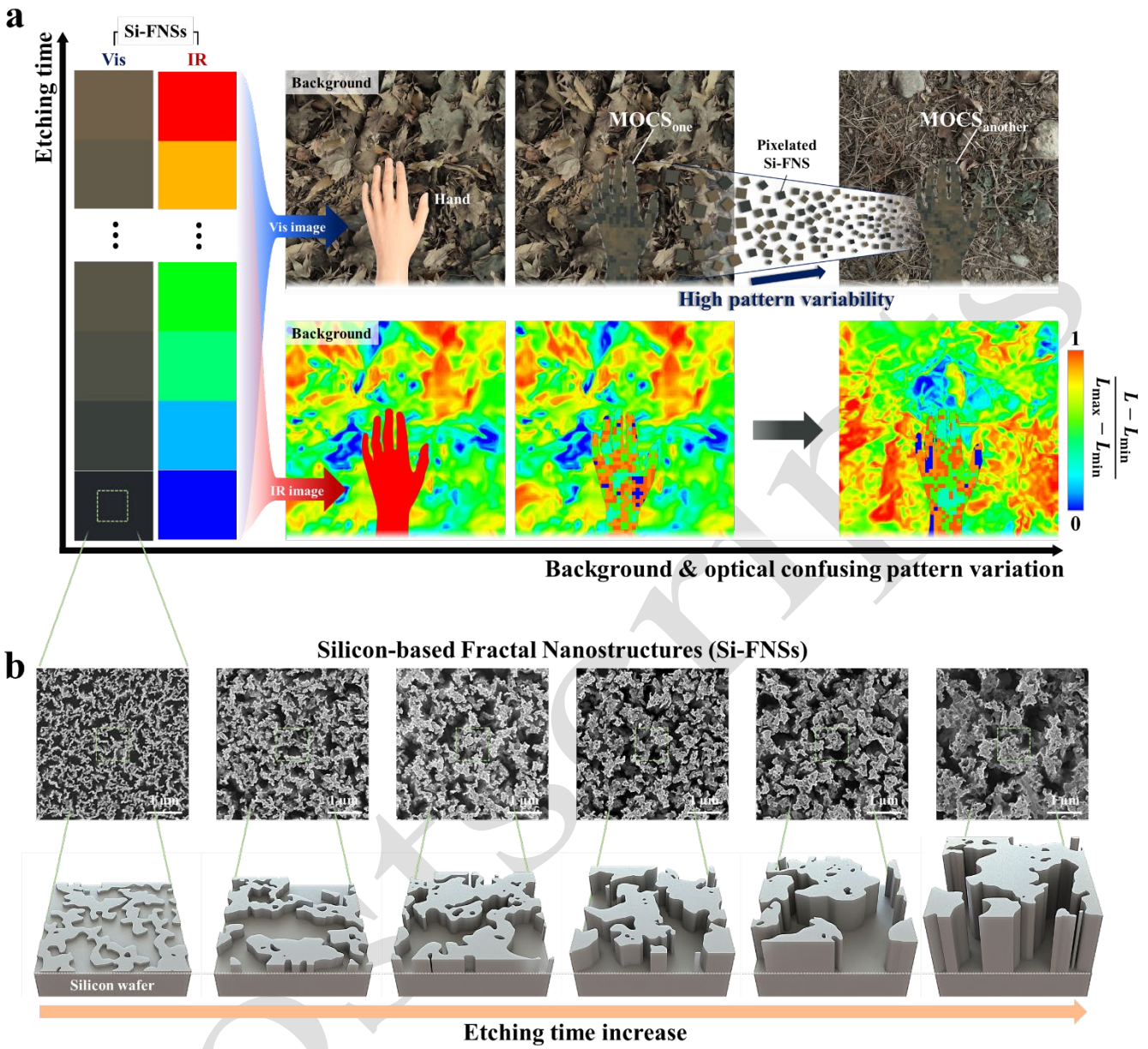

Figure 1. (a) Schematic illustration of multispectral optical confusion camouflage using MOCSs applied to the human hand. (b) the top-view SEM images (x20,000) and angled view structural schematic of fabricated Si-FNSs with etching time increase.

increased etching times result in increased heights of the Si-FNSs, and the relationship between etching time and height showed linear proportionality in this study (see Figure S1, Supporting Information). Furthermore, the sizes of the silicon nanostructure tips and cavities increase, meaning that the effective pitches and diameters of the nanostructures increase. These structural variations are attributed to the aggregation phenomenon by the Van der Waals and capillary forces, which increase as the heights of the nanostructures increase (see Note S1, Supporting Information).[34–36] Considering these facts, we believed

that the nanostructure morphologies, visible colorations, and infrared signatures were closely related. Therefore, to further understand these morphological characteristics of the Si-FNSs, we first conducted fractal analysis.

Figures 2a, 2b, and 2c show the SEM images at different magnifications for the surface morphologies of the Si-FNSs etched for 10, 50, and 240 min, respectively. First, we compared the morphological characteristics of the Si-FNSs prepared with different etching times. From the SEM images in the left column of Figures 2a-2c, all the morphologies are observed to be nearly consistent at ×10,000 magnification. This consistency is attributed to the same Ag ion concentrations of the seeding solutions used to fabricate all the Si-FNSs. The Ag ion seeding location determines where the etching occurs on the silicon substrate by the redox reaction.[37] The concentration of seeding solution determines the morphology of the silicon nanostructure.[38,39] Moreover, the morphologies of the seeded Ag particles and surface after etching for 1 min are reasonably matched with those of all the fabricated Si-FNSs (see Figure S2, Supporting Information); this similarity also supports morphological consistency. By contrast, as shown in the right column Figures 2a-2c, the sizes of the nanostructures and cavities are noticeably greater owing to the aggregation phenomenon mentioned before (Figure 1b), such that the morphological similarities between the Si-FNSs appear to decrease slightly at ×50,000 magnification. This shows that the heterogeneity or irregularity between the nanostructures increases indirectly.

Next, we compared the morphological characteristics of Si-FNSs etched for the same amount of time under different magnifications. The morphologies of the Si-FNSs show similar shapes, arrangements, and connections between the nanostructure tips, as shown in Figures 2a, 2b, and 2c, respectively. Thus, we confirmed the self-similarity characteristics reported in other finite fractal structure studies regardless of magnifications.[30,31] In the case of the short Si-FNS (Figure 2a), we observed that self-similarity was maintained regardless of the measurement position; however, owing to the considerable heterogeneities, we specially observed that the morphologies of long Si-FNSs (Figure 2c) differed slightly depending on the measurement positions (see Figure S3, Supporting Information).

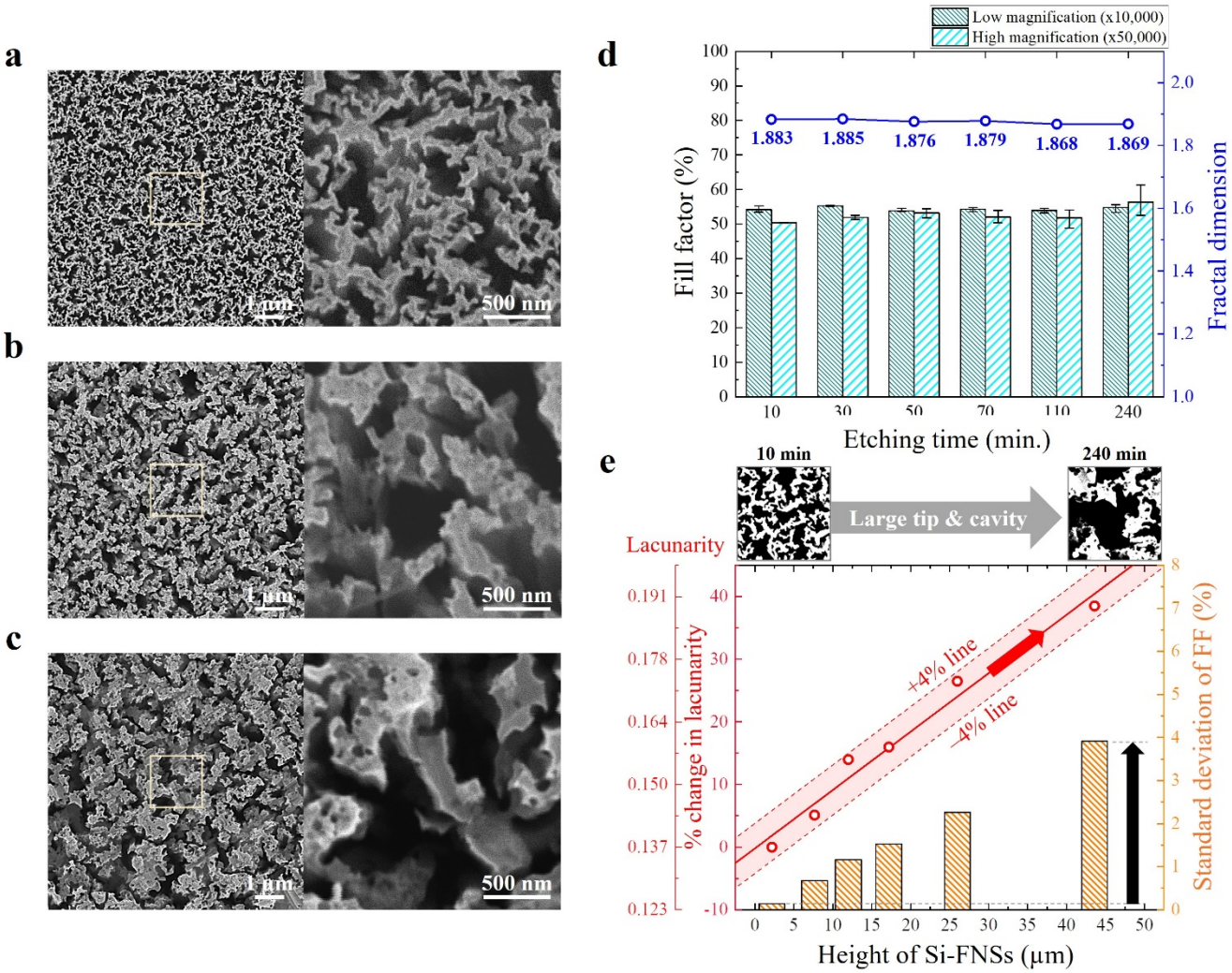

Figure 2. (a, b, and c) The top-view SEM images of the surface morphologies of the Si-FNSs etched for 10, 50, and 240 min, respectively, at different magnifications (left: ×10,000 and right: ×50,000). (d) The filling factor at different magnifications (×10,000 and ×50,000) and the fractal dimension. The error bars mean the range of estimated fill factor values. (e) The change in lacunarity and standard deviation of fill factor according to the height of Si-FNSs. The inset shows the converted binary images of Si-FNSs etched for 10 min and 240 min. The white and black colors correspond to silicon nanostructures and cavities, respectively. The side length of the inset square is 2 μm.

By confirming the inherent self-similarities of the Si-FNSs, we attempted to verify and evaluate their fractality. We estimated the fill factor (FF), which represents the surface coverage, to assess the fractality indirectly using four SEM images obtained at different positions. Additionally, we calculated the fractal dimension to verify fractal complexity (see Note S2, Supporting Information for calculation details).[40] Figure 2d shows the mean FFs at ×10,000 and ×50,000 magnifications and the fractal dimensions of the Si-FNSs depending on the etching times. The error bars represent the minimum to maximum FF values

measured at different positions. Regardless of the etching time, the FFs exhibited similar values of 54.4% and 52.6%, with relatively small standard deviations of 0.8% and 2.6% at ×10,000 and ×50,000 magnifications, respectively, compared to the mean values of the FFs. Moreover, the fractal dimensions of the fabricated Si-FNSs remain constant at 1.87, meaning that they have sufficient fractality. This value matches well with the fractal dimensions of similar silicon fractal nanostructures, i.e., silicon nanowire fractal structures, as reported in another study.[31] By assuming that this result supports the self-similarity properties and thus indicates that the Si-FNSs are finite fractal structures, we calculated the lacunarity to quantify heterogeneity and changes in the morphological characteristics of the Si-FNSs (see Note S3, Supporting Information).

Figure 2e shows the % change in lacunarity and standard deviation of the FF at ×50,000 magnification according to the heights of the Si-FNSs. The % change in lacunarity is defined as the ratio of lacunarity difference between a given Si-FNS and the shortest Si-FNS (i.e., 10 min etching case) to the lacunarity of the shortest Si-FNS. The relationship between the height of the Si-FNS and lacunarity is observed to be linear; this is because short Si-FNSs show homogeneous or uniform distributions of the nanostructure tips and cavities, but the long Si-FNS have more non-homogeneous morphologies owing to the aggregation phenomenon, as shown in the inset of Figure 2e. Therefore, the lacunarity and standard deviation of the FF increase because of this non-homogeneous morphology. The lacunarity change and standard deviation of the FF simultaneously increase up to 38.5% and 3.8%, respectively, via control of the etching time from 10 to 240 min. Associating these results with the nanostructure tip size increases by the aggregation phenomenon, the lacunarity increase indicates effective diameter as well as height increments of the Si-FNSs. Since the structural or morphological characteristics of nanostructures determine their optical characteristics,[41–43] we attempted to analyze the visible and infrared colorations to confirm the effects of fractality on the optical properties.

2.2. Visible to infrared coloration characteristics

For optical confusion camouflage in the visible range, selecting colors similar to the surrounding environment is crucial. Hence, we identified the color representations of Si-FNSs for the MOCS application. Since visible colors are determined by reflections of visible light, we conducted reflectivity measurements in the visible wavelength range of 360–780 nm. **Figure 3**a shows the reflectivity spectra of the Si-FNSs according to etching times in the visible range. Owing to the aggregation phenomenon that causes bunching of the nanostructures, Si-FNSs act like a graded-index medium[44,45] such that the Si-FNSs show lower reflectivities than the bare silicon substrate over the entire visible wavelength range, regardless of their heights (see Figure S4, Supporting Information). In particular, short Si-FNSs have strong antireflective characteristics that exhibit significantly lower reflection and higher absorption due to light-trapping effect in the subwavelength nanostructures, as reported in previous studies.[32,46–48]

On the other hand, the more etched the Si-FNS, the more is the reflectivity peak shift toward longer wavelengths before finally disappearing. The reflectivity increases over the entire visible range and particularly shows conspicuous increment in the wavelength range of approximately 500 nm or higher with increase in etching time. Similarly, the relationship between average reflectance over the visible range and lacunarity has linear proportionality, as shown in Figure 3b. As the aggregation phenomenon enlarges the tip sizes of the Si-FNSs, thus increasing lacunarity, the near-field coupling resonance shifts toward longer wavelengths and the reflection intensity increases due to enhanced refractive index mismatch within the Si-FNSs by light confinement comparable to the effective diameter.[41,44] Additionally, these near-field coupling resonances cause sharp changes in the reflectivity curve, but in the case of the Si-FNS, the reflection curve changes gradually because of bunching and disordering caused by the aggregation phenomenon[44]. Based on these principles, we conducted the numerical simulations for Si-FNSs using a simplified nanowire model with periodic boundary conditions, and the result shows good agreement with measurement (see Figure S7 and Note S7, Supporting Information). This result also supported that the reason for the reflectivity increase is due to enhanced near-field coupling between nanostructures.

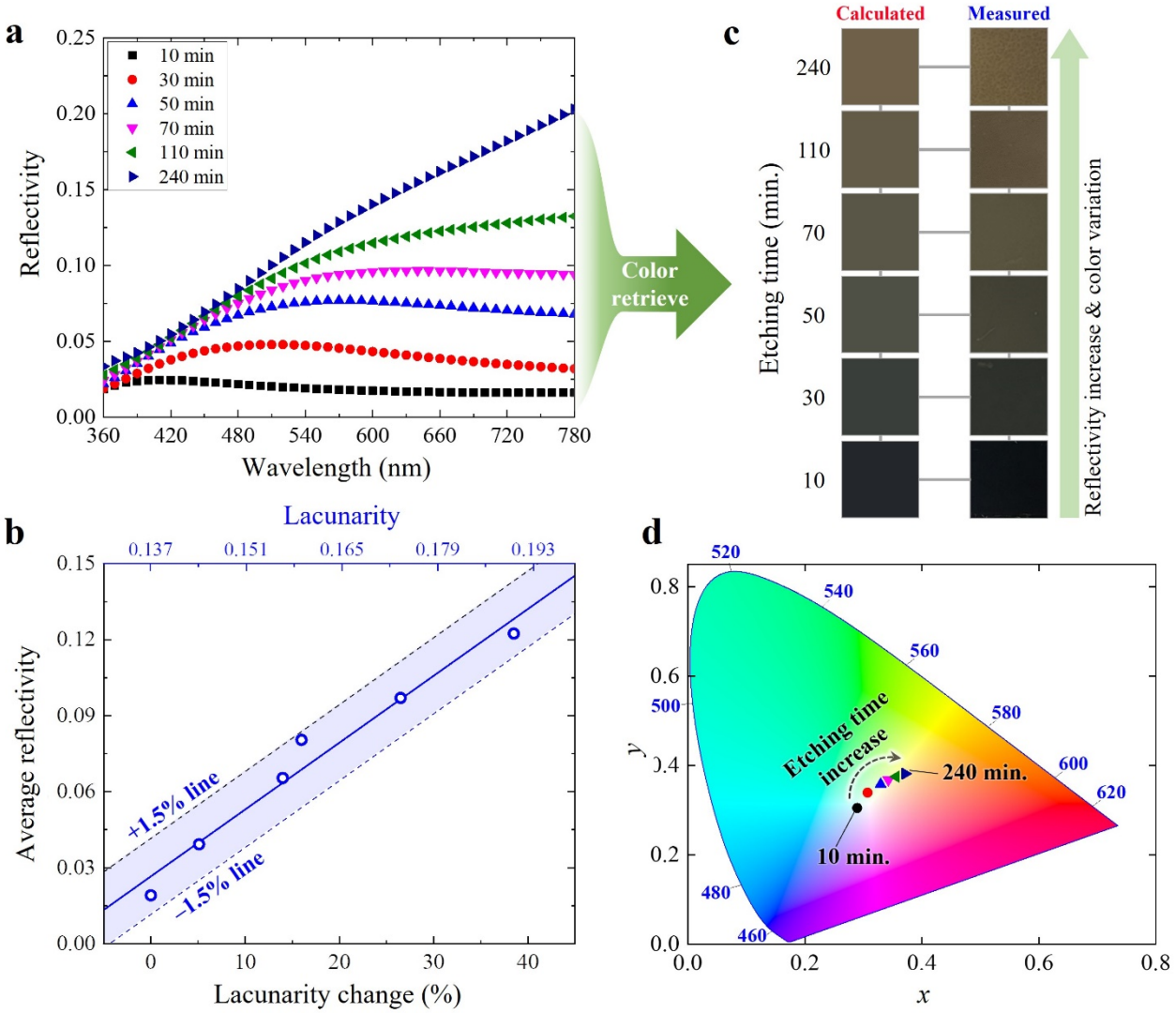

Figure 3. (a) Measured the reflectivity spectra of the Si-FNSs by etching time in the visible range. (b) The relationship between average reflectivity and lacunarity. (c) Color representation obtained from the reflectivity shown in (a) and corresponding visible images of the fabricated Si-FNSs. (d) The chromaticity coordinates of fabricated Si-FNSs on the CIE 1931 color gamut obtained from the reflectivity shown in (a). The dashed arrow indicates the etching time increase.

In addition to investigating the reflection characteristics of the Si-FNSs, we analyzed the visible colorations using the measurement results (Figure 3a) to derive a visible color palette for the MOCS design. Figure 3c shows the calculated color representations from the reflectivity measurements and their corresponding visible images for the fabricated Si-FNSs for various etching times (10–240 min). We noted that the represented colors and visible images agree well, so the MOCS pattern was designed using the color code based on the palette. Accordingly, we introduced a chromaticity coordinate to present the color

control characteristics comprehensively. Figure 3d shows the chromaticity coordinates of the fabricated Si-FNSs on the CIE 1931 color gamut obtained from the reflectivity spectra (Figure 3a). We calculated the tristimulus values to investigate the colors perceived by the human eye (see Note S4, Supporting Information for details). With increasing height, which leads to blueshift of the resonant wavelength, the color representation varies gradually from black to greens and finally to yellow (in the clockwise direction), thereby yielding a wide range of tunable colors.

Next, analogous to the fact that objects show various reflective colors in the visible range, they emit different infrared signatures. Since infrared detection systems mainly utilize the LWIR range from 8–12 μm,[49,50] we conducted imagery measurements in the LWIR range. To derive the infrared color palette corresponding to visible colors, the infrared colors representing apparent temperatures of the Si-FNSs heated to 100 ℃ were acquired with an infrared camera, which takes the signature in the LWIR range (see Experimental section for details), as shown in **Figure 4**a. Although the Si-FNSs were heated to the same temperature, the apparent temperatures increase with etching time: the apparent temperature of the Si-FNS etched for 10 min was approximately 48 ℃ but that of the Si-FNS etched for 240 min was approximately 91 ℃. Given that the emissive power is governed by the surface temperature and emissivity[8] and that the temperature of the Si-FNSs was constant, we believed that emissivity varies as the etching time increases.

Therefore, we conducted emissivity measurements in the infrared range of 8–12 μm to manipulate the infrared colors. Figure 4b shows the emissivity spectra of the Si-FNSs according to etching times in the LWIR range. Since the nanostructure layer acts as an effective medium with little resonance due to scale differences between the infrared wavelength and pitch/diameter of the nanostructures,[48] the infrared emissivity spectra are relatively flat compared with the visible reflectivity spectra. While the visible reflectivity in the long-wavelength range mainly increases (Figure 3a), the infrared emissivity increases throughout the LWIR range as etching time increases. To ensure the principle of increasing emission, we conducted the numerical simulations for Si-FNSs using a graded-index effective medium model, and the result shows good agreement with measurement (see Figure S8 and Note S7, Supporting Information).

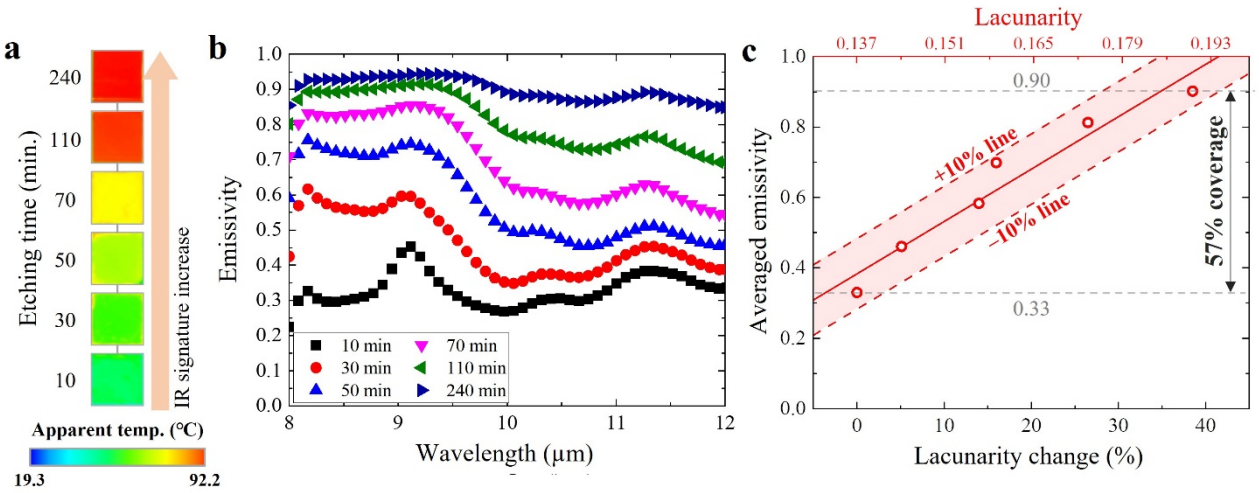

Figure 4. (a) The variation of infrared signature expressed as apparent temperature versus etching time. (b) The emissivity spectra of the Si-FNSs by etching time in the LWIR range. (c) The linear proportionality between the average emissivity in the LWIR range and the lacunarity change of the Si-FNSs.

Additionally, Figure 4c shows the relationship between the average emissivity in the LWIR range and lacunarity. As the etching time increases, the heights of the Si-FNSs increase, and the sizes of the cavities surrounded by the nanostructures also enlarge in the height direction. This structural variation improves the multiple internal reflections inside the cavity, increases the path length of the incident light, enhances the light-trapping effect in the nanostructures, and finally results in strong absorption.[32,51] Moreover, according to Kirchhoff's law,[8] emissivity and absorptivity are equal in the thermal equilibrium state, meaning that the emission increases as cavity size increases. Recalling the linear proportionality between the lacunarity and height of the Si-FNSs (Figure 2e), we observed that the average emissivity has linear proportionality with lacunarity in the LWIR range. We manipulated the average emissivity from 0.33 to 0.90 in the LWIR range by controlling the etching time and obtained 57% coverage compared to the maximum manipulation range (0–1). Therefore, we confirmed that it was possible to design and manipulate the visible reflective color and infrared emissive color simultaneously by controlling the etching time for use in the MOCS in practical applications.

2.3. Multispectral optical confusion evaluation

Before MOCS design, the infrared colors of Si-FNSs were acquired as radiance values while increasing the hotplate temperature from 40 to 100 °C. This heating temperature range represents the surface temperature determined by various environmental conditions. As shown in **Figure 5**a, the infrared color range is different for each temperature: when heated to 40 °C, the radiance changes from 37.1 to 45.6 W/m^2·sr, and when heated to 100 °C, the radiance changes in the range of 54.6 to 92.7 W/m^2·sr. This result shows the advantages of infrared signature manipulation under various temperature conditions and infers the signature controllability over wide environmental conditions. However, in terms of the infrared optical confusion against the actual environment, designing an emissivity pattern is more difficult because it is difficult to specify the temperature of the surrounding environment.

In this study, we devised a signature normalization method for the MOCS design regardless of the environmental conditions. Focusing on the fact that infrared detectors perform auto-scaling based on the maximum and minimum values of the acquired images, radiance normalization was performed for each hotplate temperature using the maximum and minimum radiances of the captured scene. This method is expressed as Equation 1.

$$\text{Normalized infrared color} = \frac{L - L_{\text{min}}}{L_{\text{Max}} - L_{\text{min}}} - (1)$$

where L denotes the surface radiance, and subscripts min and Max denote the minimum and maximum values in the captured scene, respectively. As shown in Figure 5b, we confirmed that the normalized infrared colors of all Si-FNSs were the same regardless of the hotplate temperature. Conversely, the MOCS designed with normalized infrared colors can be camouflaged well under any infrared environment.

As shown in Figures 5c and 5d, we extracted the visible and infrared camouflage patterns from the actual background images for the MOCS design. We simultaneously captured the visible and infrared images of a location in the surrounding environment, and both the infrared and visible images consisted of various colors and patterns. Considering the multicolored and patterned characteristics in the multispectral range,

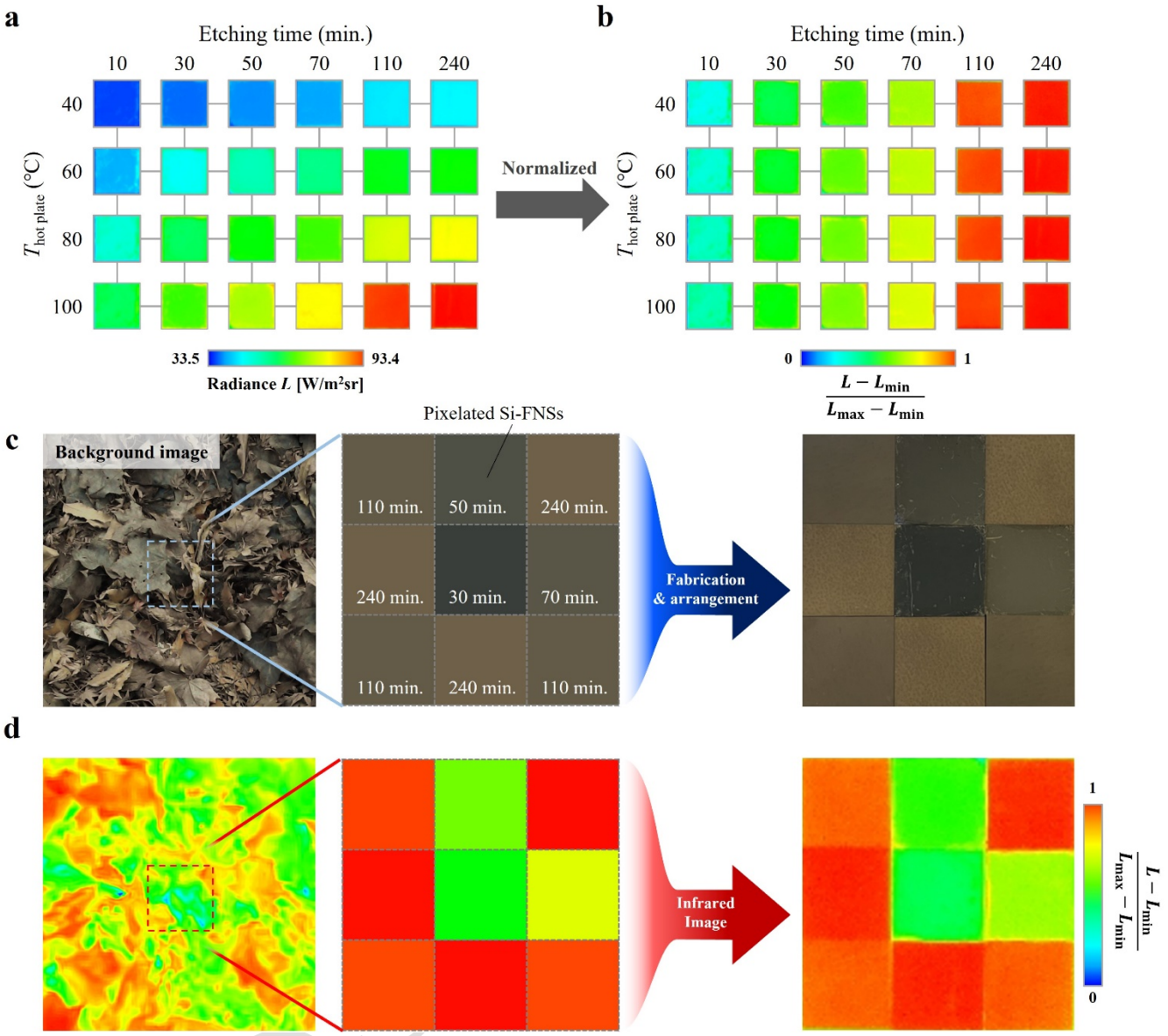

Figure 5. (a) Infrared color palette of heated Si-FNS captured by LWIR camera. The control range of the hotplate is from 40 to 100, and that of the etching time is from 10 to 240 min. (b) The normalized infrared color palette of heated Si-FNS captured by LWIR camera with the same control range. All colors in the same etching time appear the same. (c and d) the designing process of the MOCS and the images of the fabricated MOCS in the visible and infrared ranges, respectively.

we attempted to design a MOCS pattern similar to these images. The MOCS pattern consists of 3 × 3 pixels grids, with a unit pixel size of 1.5 × 1.5 cm.

To design the visible pattern of the MOCS, as shown in Figure 5c, we used the color representations of the Si-FNSs (Figure 3b). The time indicated for each pixel refers to the etching time required to fabricate the Si-FNS acquiring the designed colors. The infrared pattern designed using the corresponding normalized infrared colors also mimics the infrared background image, as shown in Figure 5d. Then, we

fabricated the MOCS to realize multispectral optical confusion effect by pixelating and arranging the Si-FNSs. As shown in the right column of Figures 5c and 5d, the images of the fabricated MOCS and designed pattern are in good agreement. Additionally, we confirmed the color repeatability/reproducibility of the Si-FNSs by comparing the individual pixels, which were independently fabricated with the same etching times.

We believed that the MOCS patterns consisting of pixelated Si-FNSs have many advantages, such as high pattern variability and effective creation of multispectral optical confusion patterns. First, the Si-FNSs were fabricated using the MaCE method, meaning that they were fabricated in a large area and cut into arbitrary pixel sizes, thus allowing generation of several Si-FNS pixels from one fabrication process. Moreover, we can generate arbitrary patterns by arranging the Si-FNS pixels by capturing and extracting the colors and patterns of various environments. On the other hand, since high-performance camouflage patterns[27,28] that can only be concealed in the visible spectral range already exist, we can effectively generate multispectral optical confusion patterns by implementing them as pixelated Si-FNSs.

Once the MOCS is created, to evaluate the multispectral optical confusion performance, we needed background panels that represent multicolored and patterned characteristics assimilated with the surrounding environment. Moreover, since different coloration principles are used to generate the visible and infrared colors (i.e., reflective and emissive, respectively), we created two artificial background panels resembling the captured environmental images in the visible and infrared ranges. We created visible-background panel (VBP) model by printing the reflective colors to represent the visible environment image; however, we created the infrared-background panel (IRBP) model using several materials with different emissivities (see Figure S5 and Note S5, Supporting Information).

Finally, we evaluated the multispectral optical confusion performance using the two model backgrounds. We also used two conventional single-spectral camouflage surfaces, namely one with a visible camouflage surface (VCS) having same visible colormap as the MOCS and the other with an infrared camouflage surface (IRCS) that lowers its emissivity to almost zero in the LWIR range using infrared selective emitter.[13,15,16] Each camouflage surface is located at the center of the VBP and IRBP in the same orientation.

Figures 6a and 6b show the multispectral images of the printed VCS. Figures 6c and 6d show the multispectral images of the fabricated IRCS, and Figures 6e and 6f show the multispectral images of the fabricated MOCS. The upper row of images (Figures 6a, 6c, and 6e) represent detection by visible seekers, and the lower row of images (Figures 6b, 6d, and 6f) represent detection by infrared seekers. Additionally, the positions of the sample surfaces are indicated by arrows and grids.

For the visible seeker, the VCS shows similar reflective color and pattern as the model background (Figure 6a). In other words, the visible camouflage surface is assimilated with the background to the extent that it is difficult to recognize the boundaries between the target surface and background, thereby indicating high optical confusion performance. However, the IRCS is significantly recognizable owing to the color and intensity gradient of gold (Au), resulting in low optical confusion performance (Figure 6c). Our MOCS shows high assimilation with the modeled background because it represents colors similar to those of the environmental elements, and it has low reflectivity owing to the antireflection properties of the Si-FNSs (Figure 6e).

Meanwhile, for the infrared seeker, both the VCS and IRCS show constant radiance values over the entire target surface and not patterned values (Figures 6b and 6d). Additionally, the VCS shows a relatively high signature, and the IRCS shows a considerably low signature compared with the IRBP. Thus, these conventional single-spectral camouflage surfaces are easily recognizable against the infrared environment. In particular, the pixel sizes comprising these surfaces are much larger than those of the background pixels, thereby resulting in low optical confusion performance.[26] However, our MOCS emits the patterned infrared signature owing to different emissivities of the individual pixels, that is, Si-FNSs with different etching times (Figure 6f). Hence, the MOCS is well-assimilated with the IRBP, showing superior optical confusion performance in the infrared range.

Overall, from the multispectral perspective, the VCS is recognizable against the infrared environment, which makes it vulnerable to infrared detectors. The IRCS is sufficiently recognizable against the visible environment and patterned infrared background because it is designed by considering the averaged

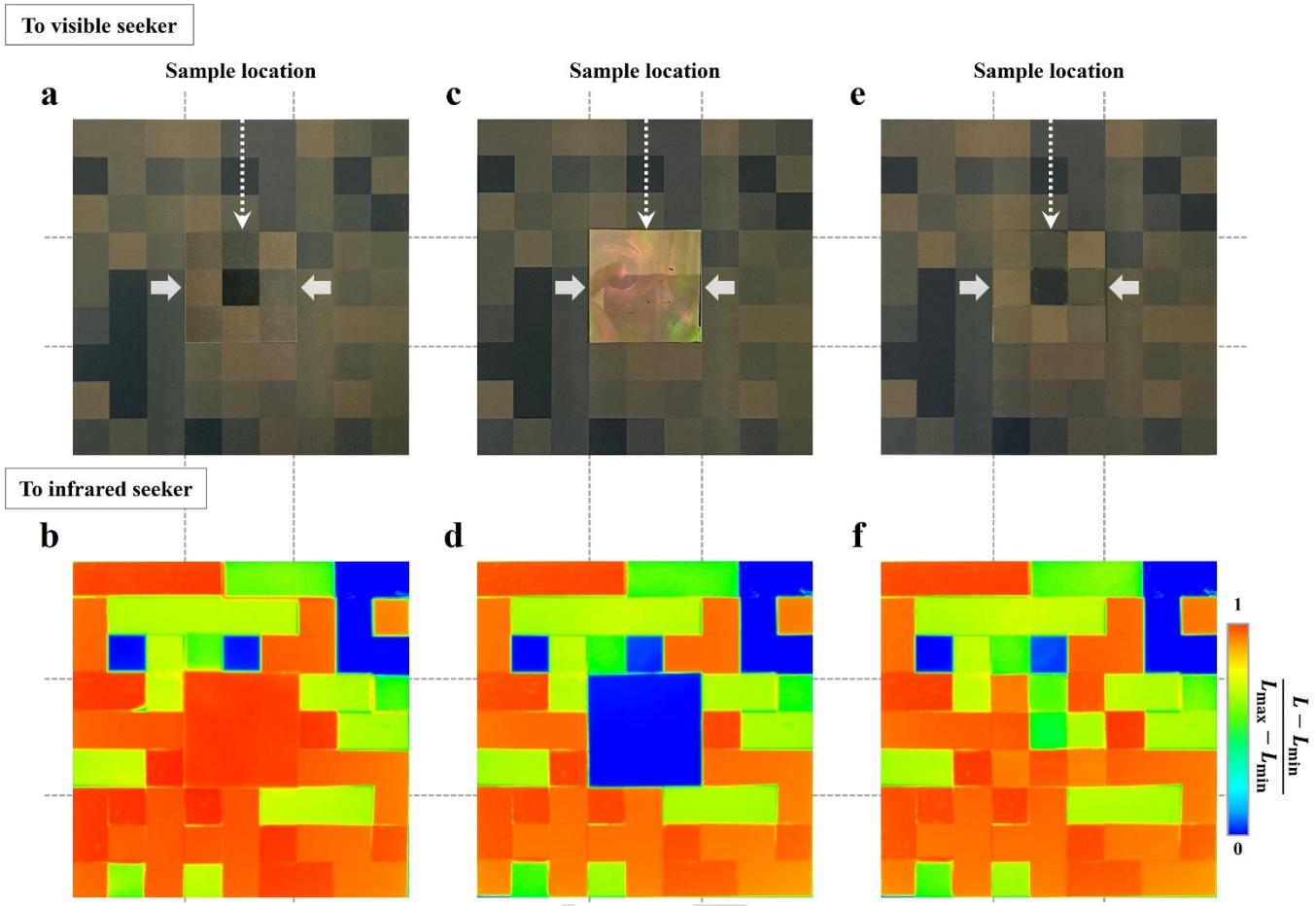

Figure 6. (a and b) The visible and infrared images of the printed visible camouflage surface with the same colormap as the MOCS, respectively. (c and d) The visible and infrared images of the fabricated infrared camouflage surface with reduced emissivity in the LWIR range, respectively. (e and f) The visible and infrared images of the fabricated MOCS, respectively. The inset arrow and grid show the sample location in the modeled backgrounds.

background signature.[13,15,16] However, our MOCS yields the highest multispectral confusion performances for all spectral ranges because we can control its color in the visible range and emission in the infrared range by controlling the etching times of the Si-FNSs. Therefore, we expect the proposed MOCS to have higher multispectral survivability than other camouflage surfaces.

3. Conclusion

In summary, we proposed a novel optical confusion camouflage system comprising several Si-FNSs as a countermeasure to multispectral imagery detectors. We demonstrated the fractal characteristics of Si-FNSs to understand the variations in the structural or morphological characteristic by the aggregation phenomenon depending on the etching times. Moreover, we demonstrated visible and infrared color palettes with pixelated Si-FNSs by calculating the visible color representations and normalizing the infrared signatures over the temperature range of 40–100 °C. The MOCS was designed and created using these palettes by extracting multispectral patterns from the actual environment images obtained simultaneously from a given location. Additionally, two model backgrounds representing the visible and infrared environmental images were fabricated by considering the color generation principles of each of the spectral ranges. We successfully demonstrated superior multispectral optical confusion performance for the MOCS with these modeled backgrounds. We expect that the MOCS proposed in this work has the potential for use in the development of stealth technology by extension of its spectral range from visible to infrared regimes, thereby deceiving state-of-the-art imagery detectors and creating variable patterns suitable for the backgrounds.

4. Methods

Fabrication of Si-FNS: To fabricate Si-FNSs, we used the MaCE method based on Ag ion reduction.[32,34,37,52] First, we cleaned a 500-μm-thick silicon substrate (p-type, 100-orientation) having resistivity between 1 and 10 Ω·cm using a plasma asher (300 W, 3 min 30 s). Next, we performed Ag ion reduction by immersing the cleaned substrate in a seeding solution (5 mM $AgNO_3$ and 4.8 M HF) for 1 min. Through this process, we could randomly "seed" the Ag ions to determine the locations where the silicon substrate was etched down. Then, we rinsed the seeded substrate with deionized (DI) water and conducted the etching process by immersing the substrate in an etchant solution (4.8 M HF and 0.1 M H_2O_2). In this process, the seeded Ag ions on the substrate acted as the cathode and the silicon substrate acted as the anode. Thus, H_2O_2 was reduced to H_2O, and silicon was oxidized and dissolved by the HF solution.[37] These redox reactions cause the silicon substrate to be etched down. Finally, we determined the height of the Si-FNSs by controlling the etching times. At the completion of the target etching time, we extracted the etched substrate and washed it with DI water. Then, we immersed the etched substrate in HNO_3 for 10 min to remove the Ag ions, rinsed it with DI water, and dried it using nitrogen gas.

Surface morphology observations: The magnified surface morphologies of the fabricated Si-FNSs were obtained by SEM (JSM-6510, JEOL). All of the fabricated Si-FNS samples were cleaned with DI water and dried using nitrogen gas before placement in the SEM equipment.

Multispectral optical property measurements: In the visible range, the optical properties were characterized using a UV-Vis-NIR spectrophotometer (Cary 5000, Agilent) equipped with an internal diffuse reflectivity accessory (DRA), which had a polytetrafluoroethylene (PTFE)-coated integrating sphere. The total reflectivity spectra were measured using this integrating sphere, which collected both the beam from the tungsten halogen source and beam reflected specularly or diffusely on the sample. An R928 photomultiplier tube (PMT) detector was used to obtain the integrated beam intensity, and the measured wavelength range was 360–780 nm. In the infrared range, the emissivity measurements were conducted using a Fourier-transform infrared (FT-IR, Vertex 70, Bruker) spectroscopy equipped with an aluminum-based

temperature-controlling accessory (A540, Bruker) for the sample as the emission source, which has sufficiently low emissivity of 0.05 or less (see Figure S6, Supporting Information for details). A deuterated L-alanine-doped triglycine sulphate (DLATGS) detector was used to determine the intensity of the emitted signal, and the measurements were obtained in the LWIR range from 8 to 12 μm. The visible reflectivity and infrared emissivity were evaluated in terms of the signal ratio between the reference and sample, that is, $\rho(\lambda_{vis},T) = R_{sample}(\lambda_{vis},T)/R_{reference}(\lambda_{vis},T)$, $\varepsilon(\lambda_{IR},T) = E_{sample}(\lambda_{IR},T)/E_{reference}(\lambda_{IR},T)$, where ρ, ε, R, E, λ, and T denote the reflectivity of the sample, emissivity of the sample, reflected energy, emitted energy, wavelength of electromagnetic waves, and temperature of the sample, respectively. The subscripts vis and IR denote visible and infrared ranges, respectively. The wavelength ranges corresponding to the above equations are 360 nm $\leq \lambda_{vis} \leq$ 780 nm and 8 μm $\leq \lambda_{IR} \leq$ 12 μm. The sample used to measure the visible reflectivity characteristics was 2 × 2 cm in size considering the aperture size of the integrated sphere, and the sample used to measure the infrared emissivity characteristics was 1.5 × 1.5 cm. The reference reflectivity was measured using a 30-mm-diameter PTFE packed diffuse reflectance disk, and the reference emissivity measurement was conducted using a cavity blackbody (SR-200, CI Systems) at the temperature of 100 ℃. *Visible and infrared image acquisitions*: For analyzing the multispectral characteristics, we measured the imagery characteristics of the pixelated Si-FNSs and MOCS. The visible images of the pixelated Si-FNSs and MOCS were acquired using a camera with the following specifications: 12 megapixels, f/1.6–2.4 aperture lens, 120° field of view, 1.4 μm pixel size, and optical image stabilization. To analyze the infrared radiative characteristics, the pixelated Si-FNSs and MOCS were attached to a 5-mm-thick copper block and heated in the range of 40–100 ℃ using a hotplate (MSH-D, DAIHAN) to ensure that the temperature of each pixel was uniform. Then, we acquired infrared images of the apparent temperature and radiance using an infrared camera (A655sc, FLIR systems) with a detection wavelength range of 8–12 μm (see Note S6, Supporting Information for details). To evaluate the optical confusion performance of the MOCS, we conducted imagery characteristics analysis using the same camera, as mentioned previously. In this study, we compared our MOCS with single-spectral camouflage surfaces, where one was a visible camouflage

surface having the same colormap as the MOCS and the other was a conventional infrared camouflage surface (that is, infrared selective emitter) that lowers the emissive power in the detection range significantly.[13,15,21] To evaluate the visible camouflages of these surfaces, we placed each surface at the center of the visible background panel consisting of reflective colors. To evaluate the infrared camouflages, we placed each surface on the infrared background panel in the same orientation as that used to evaluate the visible camouflage and heated it to 100 ℃ using the hotplate.

Supporting Information

Description of aggregation phenomenon, explanation of fractal analysis method for calculating the fractal dimension and lacunarity, derivation of CIE 1931 chromaticity coordinate for representing visible color, explanation of background modeling and fabrication, description of infrared imagery measurement, and numerical simulation of Si-FNS in the visible and infrared ranges.

Acknowledgements

This work was supported by the Aerospace Low Observable Technology Laboratory Program of the Defense Acquisition Program Administration and the Agency for Defense Development of the Republic of Korea

Author contributions

I. C., T. K., N. L., and H. H. C. designed the overall strategy. I. C., J.-S. L. and M. Y. fabricated the samples. I. C., J. N., and J.-S. L. measured the spectral reflectivity and emissivity through the UV-vis-NIR spectrophotometer and FT-IR facility. I. C., N. L., and J. N. performed fractality calculation for revealing morphological characteristics. I. C. and J. N. captured the visible and infrared images to evaluate the camouflage performance. All the authors analyzed the data. I. C. and H. H. C. wrote and supervised the manuscript.

References

(1) Xu, C.; Colorado Escobar, M.; Gorodetsky, A. A. Stretchable Cephalopod-Inspired Multimodal Camouflage Systems. *Adv. Mater.* **2020**, *32* (16), 1905717. https://doi.org/10.1002/adma.201905717.

(2) Zhang, Z. L.; Dong, X.; Fan, Y. N.; Yang, L. M.; He, L.; Song, F.; Wang, X. L.; Wang, Y. Z. Chameleon-Inspired Variable Coloration Enabled by a Highly Flexible Photonic Cellulose Film. *ACS Appl. Mater. Interfaces* **2020**, *12* (41), 46710–46718. https://doi.org/10.1021/acsami.0c13551.

(3) Malchow, D.; Battaglia, J.; Brubaker, R.; Ettenberg, M. High Speed Short Wave Infrared (SWIR) Imaging and Range Gating Cameras. *Thermosense XXIX* **2007**, *6541* (April 2007), 654106. https://doi.org/10.1117/12.721747.

(4) Bowman, A. J.; Klopfer, B. B.; Juffmann, T.; Kasevich, M. A. Electro-Optic Imaging Enables Efficient Wide-Field Fluorescence Lifetime Microscopy. *Nat. Commun.* **2019**, *10* (1), 4561. https://doi.org/10.1038/s41467-019-12535-5.

(5) Türker-Kaya, S.; Huck, C. W. A Review of Mid-Infrared and near-Infrared Imaging: Principles, Concepts and Applications in Plant Tissue Analysis. *Molecules* **2017**, *22* (1), 168. https://doi.org/10.3390/molecules22010168.

(6) Park, H.; Crozier, K. B. Multispectral Imaging with Vertical Silicon Nanowires. *Sci. Rep.* **2013**, *3*, 2460. https://doi.org/10.1038/srep02460.

(7) Kim, S.; Song, W. J.; Kim, S. H. Robust Ground Target Detection by SAR and IR Sensor Fusion Using Adaboost-Based Feature Selection. *Sensors (Switzerland)* **2016**, *16* (7), 1–27. https://doi.org/10.3390/s16071117.

(8) Modest, M. F. Chapter 3 - Radiative Properties of Real Surfaces. In *Radiative Heat Transfer (Third Edition)*; Modest, M. F., Ed.; Academic Press: Boston, 2013; pp 61–128. https://doi.org/https://doi.org/10.1016/B978-0-12-386944-9.50003-0.

(9) Li, M.; Liu, D.; Cheng, H.; Peng, L.; Zu, M. Manipulating Metals for Adaptive Thermal Camouflage. *Sci. Adv.* **2020**, *6* (22), eaba3494. https://doi.org/10.1126/sciadv.aba3494.

(10) Yoon, G.; Kim, K.; Huh, D.; Lee, H.; Rho, J. Single-Step Manufacturing of Hierarchical Dielectric Metalens in the Visible. *Nat. Commun.* **2020**, *11* (1), 2268. https://doi.org/10.1038/s41467-020-16136-5.

(11) Kim, Y. J.; Yoo, Y. J.; Lee, G. J.; Yoo, D. E.; Lee, D. W.; Siva, V.; Song, H.; Kang, I. S.; Song, Y. M. Enlarged Color Gamut Representation Enabled by Transferable Silicon Nanowire Arrays on Metal-Insulator-Metal Films. *ACS Appl. Mater. Interfaces* **2019**, *11* (12), 11849–11856. https://doi.org/10.1021/acsami.8b21554.

(12) Jin, Y.; Jin, Y.; Baugh, N.; Lin, Y.; Ge, M.; Dickey, M. D.; Dickey, M. D. Soft, Stretchable, and Pneumatically Triggered Thermochromic Optical Filters with Embedded Phosphorescence. *ACS Appl. Mater. Interfaces* **2020**, *12* (23), 26424–26431. https://doi.org/10.1021/acsami.0c03655.

(13) Lee, N.; Yoon, B.; Kim, T.; Bae, J. Y.; Lim, J. S.; Chang, I.; Cho, H. H. Multiple Resonance Metamaterial Emitter for Deception of Infrared Emission with Enhanced Energy Dissipation. *ACS Appl. Mater. Interfaces* **2020**, *12* (7), 8862–8869. https://doi.org/10.1021/acsami.9b21030.

(14) Lee, N.; Lim, J. S.; Chang, I.; Lee, D.; Cho, H. H. Flexible Thermocamouflage Materials in Supersonic Flowfields with Selective Energy Dissipation. *ACS Appl. Mater. Interfaces* **2021**. https://doi.org/10.1021/acsami.1c09333.

(15) Lee, N.; Kim, T.; Lim, J. S.; Chang, I.; Cho, H. H. Metamaterial-Selective Emitter for Maximizing Infrared Camouflage Performance with Energy Dissipation. *ACS Appl. Mater. Interfaces* **2019**, *11* (23), 21250–21257. https://doi.org/10.1021/acsami.9b04478.

(16) Zhu, H.; Li, Q.; Zheng, C.; Hong, Y.; Xu, Z.; Wang, H.; Shen, W.; Kaur, S.; Ghosh, P.; Qiu, M. High-Temperature Infrared Camouflage with Efficient Thermal Management. *Light Sci. Appl.* **2020**, *9* (1), 60. https://doi.org/10.1038/s41377-020-0300-5.

(17) Peng, L.; Liu, D.; Cheng, H.; Zhou, S.; Zu, M. A Multilayer Film Based Selective Thermal Emitter for Infrared Stealth Technology. *Adv. Opt. Mater.* **2018**, *6* (23), 1801006. https://doi.org/10.1002/adom.201801006.

(18) Zhu, H.; Li, Q.; Tao, C.; Hong, Y.; Xu, Z.; Shen, W.; Kaur, S.; Ghosh, P.; Qiu, M. Multispectral Camouflage for Infrared, Visible, Lasers and Microwave with Radiative Cooling. *Nat. Commun.* **2021**, *12* (1), 1805. https://doi.org/10.1038/s41467-021-22051-0.

(19) Zhang, J.; Zhang, J.; Ou, Y.; Qin, Y.; Wen, H.; Dong, W.; Wang, R.; Chen, S.; Yu, Z. Photonic Plasticines with Uniform Structural Colors, High Processability, and Self-Healing Properties. *Small* **2021**, *17* (8), 2007426. https://doi.org/10.1002/smll.202007426.

(20) Chen, S.; Haehnle, B.; Van der Laan, X.; Kuehne, A. J. C.; Botiz, I.; Stavrinou, P. N.; Stingelin, N. Understanding Hierarchical Spheres-in-Grating Assembly for Bio-Inspired Colouration. *Mater. Horizons* **2021**, *8* (8), 2230–2237. https://doi.org/10.1039/d1mh00358e.

(21) Kim, T.; Bae, J. Y.; Lee, N.; Cho, H. H. Hierarchical Metamaterials for Multispectral Camouflage of Infrared and Microwaves. *Adv. Funct. Mater.* **2019**, *29* (10), 1807319. https://doi.org/10.1002/adfm.201807319.

(22) Lee, N.; Lim, J. S.; Chang, I.; Lee, D.; Cho, H. H. Transparent Metamaterials for Multispectral Camouflage with Thermal Management. *Int. J. Heat Mass Transf.* **2021**, *173*. https://doi.org/10.1016/j.ijheatmasstransfer.2021.121173.

(23) Barho, F. B.; Gonzalez-Posada, F.; Cerutti, L.; Taliercio, T. Heavily Doped Semiconductor Metamaterials for Mid-Infrared Multispectral Perfect Absorption and Thermal Emission. *Adv. Opt. Mater.* **2020**, *8* (6), 1901502. https://doi.org/10.1002/adom.201901502.

(24) Lee, J.; Sul, H.; Jung, Y.; Kim, H.; Han, S.; Choi, J.; Shin, J.; Kim, D.; Jung, J.; Hong, S.; Ko, S. H. Thermally Controlled, Active Imperceptible Artificial Skin in Visible-to-Infrared Range. *Adv. Funct. Mater.* **2020**, *30* (36), 1–11. https://doi.org/10.1002/adfm.202003328.

(25) Xu, Z.; Luo, H.; Zhu, H.; Hong, Y.; Shen, W.; Ding, J.; Kaur, S.; Ghosh, P.; Qiu, M.; Li, Q. Nonvolatile Optically Reconfigurable Radiative Metasurface with Visible Tunability for Anticounterfeiting. *Nano Lett.* **2021**, *21* (12), 5269–5276. https://doi.org/10.1021/acs.nanolett.1c01396.

(26) Cheng, X. peng; Zhao, D. peng; Yu, Z. jie; Zhang, J. hua; Bian, J. tian; Yu, D. bin. Effectiveness Evaluation of Infrared Camouflage Using Image Saliency. *Infrared Phys. Technol.* **2018**, *95* (June), 213–221. https://doi.org/10.1016/j.infrared.2018.11.001.

(27) Xiao, H.; Qu, Z.; Lv, M.; Jiang, Y.; Wang, C.; Qin, R. Fast Self-Adaptive Digital Camouflage Design Method Based on Deep Learning. *Appl. Sci.* **2020**, *10* (15), 5284. https://doi.org/10.3390/APP10155284.

(28) Yang, X.; Xu, W. D.; Jia, Q.; Li, L. Research on Digital Camouflage Pattern Generation Algorithm Based on Adversarial Autoencoder Network. *Int. J. Pattern Recognit. Artif. Intell.* **2020**, *34* (6), 2050017. https://doi.org/10.1142/S0218001420500172.

(29) Peng, K. Q.; Yan, Y. J.; Gao, S. P.; Zhu, J. Synthesis of Large-Area Silicon Nanowire Arrays via Self-Assembling Nanoelectrochemistry. *Adv. Mater.* **2002**, *14* (16), 1164–1167. https://doi.org/10.1002/1521-4095(20020816)14:16<1164::AID-ADMA1164>3.0.CO;2-E.

(30) Lo Faro, M. J.; Leonardi, A. A.; Priolo, F.; Fazio, B.; Miritello, M.; Irrera, A. Erbium Emission in Er:Y2O3 Decorated Fractal Arrays of Silicon Nanowires. *Sci. Rep.* **2020**, *10* (1), 12854. https://doi.org/10.1038/s41598-020-69864-5.

(31) Fazio, B.; Artoni, P.; Iatì, M. A.; D'andrea, C.; Lo Faro, M. J.; Sorbo, S. Del; Pirotta, S.; Gucciardi, P. G.; Musumeci, P.; Vasi, C. S.; Saija, R.; Galli, M.; Priolo, F.; Irrera, A. Strongly Enhanced Light Trapping in a Two-Dimensional Silicon Nanowire Random Fractal Array. *Light Sci. Appl.* **2016**, *5*, e16062. https://doi.org/10.1038/lsa.2016.62.

(32) Kim, B. S.; Tamboli, S. H.; Han, J. B.; Kim, T.; Cho, H. H. Broadband Radiative Energy Absorption Using a Silicon Nanowire Forest with Silver Nanoclusters for Thermal Energy

Conversion. *Int. J. Heat Mass Transf.* **2015**, *82*, 267–272. https://doi.org/10.1016/j.ijheatmasstransfer.2014.11.043.

(33) Dasgupta, N. P.; Sun, J.; Liu, C.; Brittman, S.; Andrews, S. C.; Lim, J.; Gao, H.; Yan, R.; Yang, P. 25th Anniversary Article: Semiconductor Nanowires - Synthesis, Characterization, and Applications. *Adv. Mater.* **2014**, *26* (14), 2137–2184. https://doi.org/10.1002/adma.201305929.

(34) Shim, D. Il; Choi, G.; Lee, N.; Kim, T.; Kim, B. S.; Cho, H. H. Enhancement of Pool Boiling Heat Transfer Using Aligned Silicon Nanowire Arrays. *ACS Appl. Mater. Interfaces* **2017**, *9* (20), 17595–17602. https://doi.org/10.1021/acsami.7b01929.

(35) Zhu, K.; Vinzant, T. B.; Neale, N. R.; Frank, A. J. Removing Structural Disorder from Oriented TiO2 Nanotube Arrays: Reducing the Dimensionality of Transport and Recombination in Dye-Sensitized Solar Cells. *Nano Lett.* **2007**, *7* (12), 3739–3746. https://doi.org/10.1021/nl072145a.

(36) Khorasaninejad, M.; Abedzadeh, N.; Singh Jawanda, A.; Nixon, O.; Anantram, M. P.; Singh Saini, S. Bunching Characteristics of Silicon Nanowire Arrays. *J. Appl. Phys.* **2012**, *111* (4). https://doi.org/10.1063/1.3688025.

(37) Huang, Z.; Geyer, N.; Werner, P.; De Boor, J.; Gösele, U. Metal-Assisted Chemical Etching of Silicon: A Review. *Adv. Mater.* **2011**, *23* (2), 285–308. https://doi.org/10.1002/adma.201001784.

(38) Swarnalatha, V.; Narasimha Rao, A. V.; Pal, P. Effective Improvement in the Etching Characteristics of Si{110} in Low Concentration TMAH Solution. *Micro Nano Lett.* **2018**, *13* (8), 1085–1089. https://doi.org/10.1049/mnl.2017.0610.

(39) Tsujino, K.; Matsumura, M. Morphology of Nanoholes Formed in Silicon by Wet Etching in Solutions Containing HF and H2O2 at Different Concentrations Using Silver Nanoparticles as Catalysts. *Electrochim. Acta* **2007**, *53* (1), 28–34. https://doi.org/10.1016/j.electacta.2007.01.035.

(40) Ayan, B.; Heo, D. N.; Zhang, Z.; Dey, M.; Povilianskas, A.; Drapaca, C.; Ozbolat, I. T. Aspiration-Assisted Bioprinting for Precise Positioning of Biologics. *Sci. Adv.* **2020**, *6* (10), eaaw5111. https://doi.org/10.1126/sciadv.aaw5111.

(41) Khorasaninejad, M.; Abedzadeh, N.; Walia, J.; Patchett, S.; Saini, S. S. Color Matrix Refractive Index Sensors Using Coupled Vertical Silicon Nanowire Arrays. *Nano Lett.* **2012**, *12* (8), 4228–4234. https://doi.org/10.1021/nl301840y.

(42) Wendisch, F. J.; Abazari, M.; Mahdavi, H.; Rey, M.; Vogel, N.; Musso, M.; Diwald, O.; Bourret, G. R. Morphology-Graded Silicon Nanowire Arrays via Chemical Etching: Engineering Optical Properties at the Nanoscale and Macroscale. *ACS Appl. Mater. Interfaces* **2020**, *12* (11), 13140–13147. https://doi.org/10.1021/acsami.9b21466.

(43) Ravishankar, A. P.; Van Tilburg, M. A. J.; Vennberg, F.; Visser, D.; Anand, S. Color Generation from Self-Organized Metalo-Dielectric Nanopillar Arrays. *Nanophotonics* **2019**, *8* (10), 1771–1781. https://doi.org/10.1515/nanoph-2019-0171.

(44) Khorasaninejad, M.; Patchett, S.; Sun, J.; O, N.; Saini, S. S. Polarization-Resolved Reflections in Ordered and Bunched Silicon Nanowire Arrays. *J. Opt. Soc. Am. B* **2012**, *29* (11), 3063–3068. https://doi.org/10.1364/JOSAB.29.003063.

(45) Hsu, S. H.; Liu, E. S.; Chang, Y. C.; Hilfiker, J. N.; Kim, Y. D.; Kim, T. J.; Lin, C. J.; Lin, G. R. Characterization of Si Nanorods by Spectroscopic Ellipsometry with Efficient Theoretical Modeling. *Phys. Status Solidi Appl. Mater. Sci.* **2008**, *205* (4), 876–879. https://doi.org/10.1002/pssa.200777832.

(46) Zhu, J.; Yu, Z.; Burkhart, G. F.; Hsu, C. M.; Connor, S. T.; Xu, Y.; Wang, Q.; McGehee, M.; Fan, S.; Cui, Y. Optical Absorption Enhancement in Amorphous Silicon Nanowire and Nanocone Arrays. *Nano Lett.* **2009**, *9* (1), 279–282. https://doi.org/10.1021/nl802886y.

(47) Garnett, E.; Yang, P. Light Trapping in Silicon Nanowire Solar Cells. *Nano Lett.* **2010**, *10* (3), 1082–1087. https://doi.org/10.1021/nl100161z.

(48) Steglich, M.; Käsebier, T.; Schrempel, F.; Kley, E. B.; Tünnermann, A. Self-Organized, Effective Medium Black Silicon for Infrared Antireflection. *Infrared Phys. Technol.* **2015**, *69*, 218–221. https://doi.org/10.1016/j.infrared.2015.01.033.

(49) Pan, M.; Huang, Y.; Li, Q.; Luo, H.; Zhu, H.; Kaur, S.; Qiu, M. Multi-Band Middle-Infrared-Compatible Camouflage with Thermal Management via Simple Photonic Structures. *Nano Energy* **2020**, *69* (August), 104449. https://doi.org/10.1016/j.nanoen.2020.104449.

(50) Kim, T.; Lee, H.; Bae, J. Y.; Kim, T.; Cha, J.; Jung, D.; Cho, H. H. Susceptibility of Combat Aircraft Modeled as an Anisotropic Source of Infrared Radiation. *IEEE Trans. Aerosp. Electron. Syst.* **2016**, *52* (5), 2467–2476. https://doi.org/10.1109/TAES.2016.150513.

(51) Wu, C.; Geng, H.; Tan, S.; Lv, J.; Wang, H.; He, Z.; Wang, J. Highly Efficient Solar Anti-Icing/Deicing: Via a Hierarchical Structured Surface. *Mater. Horizons* **2020**, *7* (8), 2097–2104. https://doi.org/10.1039/d0mh00636j.

(52) Kim, B. S.; Shin, S.; Shin, S. J.; Kim, K. M.; Cho, H. H. Control of Superhydrophilicity/Superhydrophobicity Using Silicon Nanowires via Electroless Etching Method and Fluorine Carbon Coatings. *Langmuir* **2011**, *27* (16), 10148–10156. https://doi.org/10.1021/la200940j.

Table of Contents (ToCs)